

Design and Calibration of the 34 GHz Yale Microwave Cavity Experiment

P. L. Slocum^a, O. K. Baker^a, J. L. Hirshfield^{a,b}, Y. Jiang^a, A. T. Malagon^a,
A. J. Martin^a, S. Shchelkunov^a, A. Szymkowiak^{a,c}

^a*Department of Physics, Yale University, PO Box 208120, New Haven, CT USA 06520*

^b*Omega-P, Inc., 291 Whitney Ave., Suite 401, New Haven, CT 06511*

^c*Department of Astronomy, Yale University, PO Box 208101, New Haven CT 06520*

Abstract

Several proposed models of the cold dark matter in the universe include light neutral bosons with sub-eV masses. In many cases their detection hinges on their infrequent interactions with Standard Model photons at sub-eV energies. We describe the design and performance of an experiment to search for aberrations from the broadband noise power associated with a 5 K copper resonant cavity in the vicinity of 34 GHz (0.1 meV). The cavity, microwave receiver, and data reduction are described. Several configurations of the experiment are discussed in terms of their impact on the sensitivity of the search for axion-like particles and hidden sector photons.

Keywords: resonant cavity, microwave receiver, axion, cold dark matter, hidden sector photon

1. Introduction

Direct detection of cold dark matter (CDM) is required before many questions can be addressed about its origin and implications in the universe. Cosmological evidence for the existence of dark matter [1, 2, 3, 4] has consistently driven the need for measurements that can impose additional constraints on theory.

Searches for CDM with masses of GeV/c² are ongoing but have thus far yielded either inconclusive [5, 6, 7, 8, 9] or negative results [10, 11, 12, 13, 14, 15]. Similarly, collider searches for signals from CDM have been negative [16]. These measurements have led to constructive limits on models as well as a heightened interest in light CDM candidates with masses less than 1 eV.

Thus far searches for light CDM in the laboratory have focused primarily on particles that should interact infrequently, but predictably, with Standard Model (SM) photons. The pseudoscalar axion [17, 18, 19] is required to couple to 2 SM photons by way of the Primakoff effect. Other pseudoscalar and scalar axion-like particles (ALPs) that arise in string theory [20, 21] are allowed, but not required, to couple to 2 photons. The vector hidden sector photon [20, 21] can also be the CDM [22, 21] and interacts with SM photons through mass-dependent kinetic mixing.

The nearly monoenergetic distribution of light CDM, as well as its possible interaction with sub-eV (\lesssim GHz) photons, make it susceptible to discovery in searches that utilize radio frequency (RF) detection techniques. In particular, the approach pioneered by Sikivie [23, 24] and the ADMX collaboration [25, 26, 27] in which a resonant cavity sitting in a strong magnetic field is coupled to a microwave receiver can be an extremely sensitive probe of the sub-eV mass regime [27]. In this paper we discuss the design and calibration of a similar experiment. A low-noise cryogenic amplifier and microwave receiver are employed to search for deviations from the nominal spectrum of 34 GHz power associated with a 5 K Cu resonant cavity. Several configurations of the experiment are discussed in terms of their sensitivity to sub-eV mass CDM models.

2. Experiment

2.1. Magnet and Cryostat

The experiment sits inside an Oxford Instruments V22460 superconducting magnet with a peak field of 7 T inside the warm bore of diameter 89 mm. The magnetic field is strongest in a 10 cm long region located 36 cm above the bottom edge of the bore. The intended purpose of the magnet is for measurements of nuclear magnetic resonance (NMR) with a field that is specified to be uniform across the peak region to a few parts per million. In the present experiment, however, the field uniformity is only required to be of order 10%. The temporal stability of the field has been found to be better than a few percent over a span of 5 years. An outline of the magnet is included in Figure 1.

Also shown in Figure 1 is the liquid He cryostat system that extends into the bore of the magnet. Its central sample tube houses the signal cavity and cryogenic amplifiers, and is cooled by He gas that has been vaporized from a reservoir of liquid He. Surrounding the sample tube is a liquid N₂

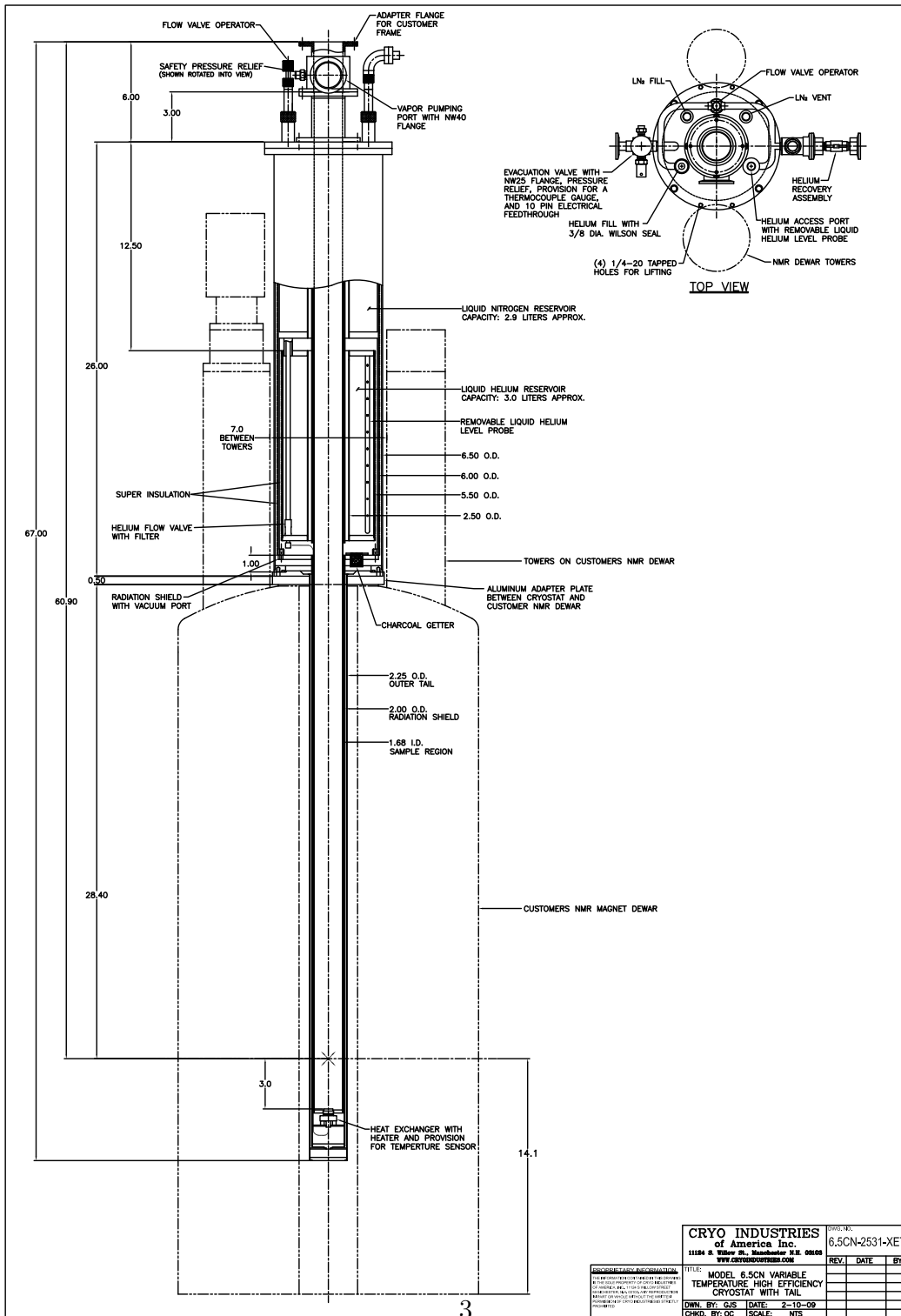


Figure 1: Magnet, built by Oxford Instruments, and cold gas cryostat built by Cryo Industries of America, Inc.

thermal radiation shield. The inner diameter of the sample region is 4.27 cm and is limited by the diameter of the bore of the magnet and the size of the room-temperature drive cavity. The physical temperatures at the cavity, amplifiers, and vaporizer are monitored with thin-film resistance cryogenic temperature sensors made by Lake Shore Cryotronics, Inc.

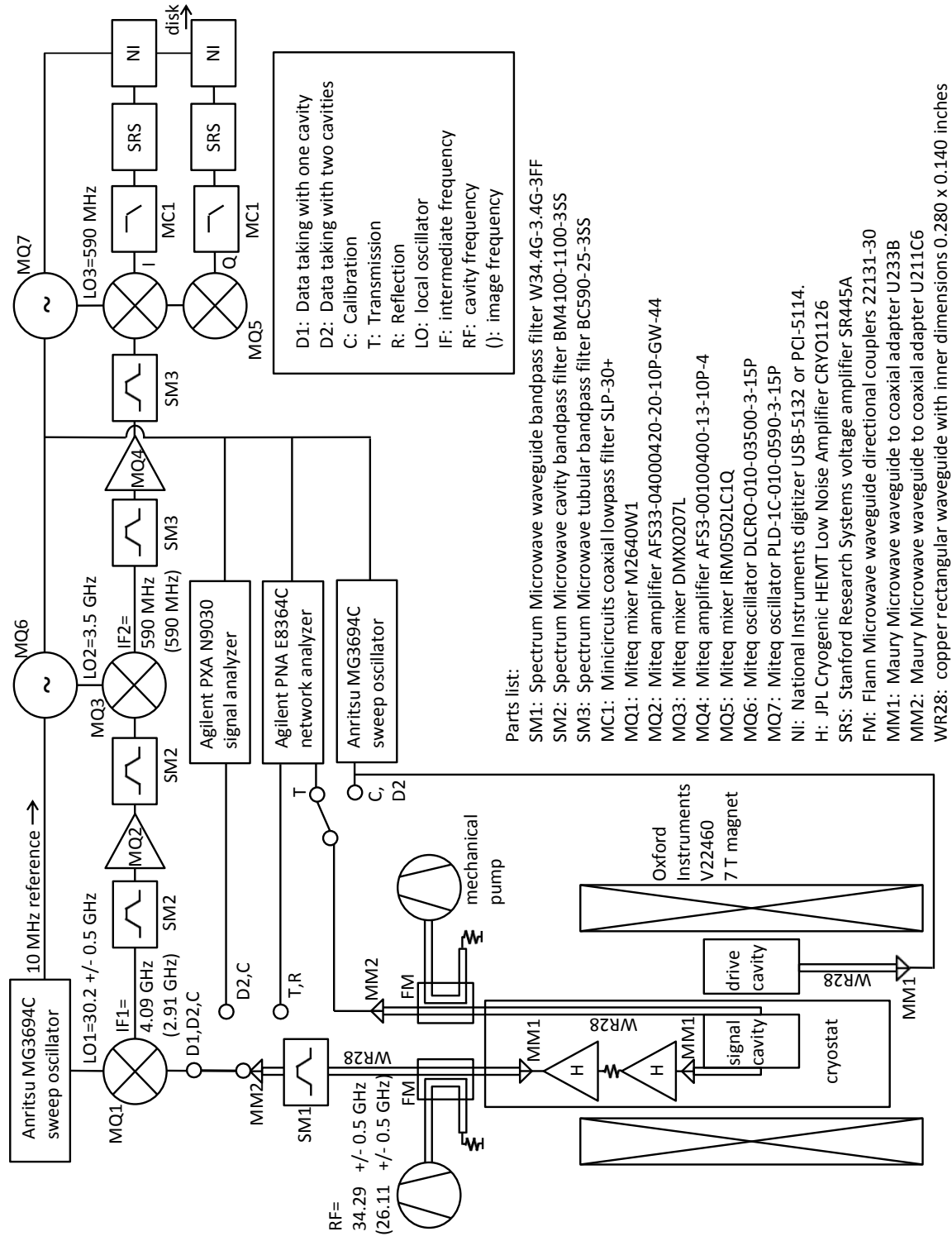
2.2. Copper Resonant Cavities

The experiment has two main running configurations: an experiment that is driven with 34 GHz RF power, and alternatively, a listening mode. The driven experiment consists of two adjacent 34 GHz oxygen-free high thermal conductivity (OFHC) copper microwave cavities each of which supports a transverse electric (TE) mode. The “signal” cavity sits near the bottom of the cryostat in the region where the external B-field is maximal. The “drive” cavity sits adjacent to the signal cavity, inside the bore of the magnet but outside the cryostat. In the second configuration, or listening mode, only the signal cavity is employed. One of two types of signal cavities is utilized: Either a cavity that supports a TE mode, or one that supports the transverse magnetic (TM) mode. The locations of the signal and drive cavities are shown in the schematic of Figure 2.

2.2.1. Signal Cavities

The cylindrical TE signal cavity supports the TE_{011} mode and is 11 mm in diameter by 17 mm in height. Its central resonant frequency is 34.29 GHz. The resonant frequency is tunable across 500 MHz using a plunger that moves vertically. There is a 1 mm gap between the plunger and the side wall whose purpose is to break the degeneracy between the TE_{011} and the TM_{111} modes. The position of the plunger is adjusted by a lever attached to a threaded fitting that moves freely at temperatures between 7 K and 300 K. The fitting attaches to a meter-long fiberglass G10 rod that is turned by hand from outside the top flange of the cryostat. Figure 3 shows a drawing of the TE_{011} cavity and its tuning mechanism. Also shown are the thin OFHC fins that increase the surface area of the assembly, helping to optimize its rate of cooling inside the cryostat. The fins are asymmetric due to constraints on available space.

The TE_{011} signal cavity is designed to be critically coupled at cryogenic temperatures to a few inches of copper rectangular WR28 waveguide. The waveguide has inside dimensions 0.280 by 0.140 inches and cutoff frequency



Parts list:

SM1: Spectrum Microwave waveguide bandpass filter W34.4G-3.4G-3FF
 SM2: Spectrum Microwave cavity bandpass filter BM4100-1100-3SS
 SM3: Spectrum Microwave tubular bandpass filter BC590-25-3SS
 MC1: Minircuits coaxial lowpass filter SLP-30+
 MQ1: Miteq mixer M2640W1
 MQ2: Miteq amplifier AFS33-04000420-20-10P-GW-44
 MQ3: Miteq mixer DMX0207L
 MQ4: Miteq amplifier AFS3-00100400-13-10P-4
 MQ5: Miteq mixer IRM0502LC1Q
 MQ6: Miteq oscillator DLCRO-010-03500-3-15P
 MQ7: Miteq oscillator PLD-1C-010-0590-3-15P
 NI: National Instruments digitizer USB-5132 or PCI-5114.
 H: JPL Cryogenic HEMT Low Noise Amplifier CRYO1126
 SRS: Stanford Research Systems voltage amplifier SR445A
 FM: Flann Microwave waveguide directional couplers 22131-30
 MM1: Maury Microwave waveguide to coaxial adapter U233B
 MM2: Maury Microwave waveguide to coaxial adapter U211C6
 WR28: copper rectangular waveguide with inner dimensions 0.280 x 0.140 inches

D1: Data taking with one cavity
 D2: Data taking with two cavities
 C: Calibration
 T: Transmission
 R: Reflection
 LO: local oscillator
 IF: intermediate frequency
 RF: cavity frequency
 (:): image frequency

Figure 2: Schematic of the experiment.

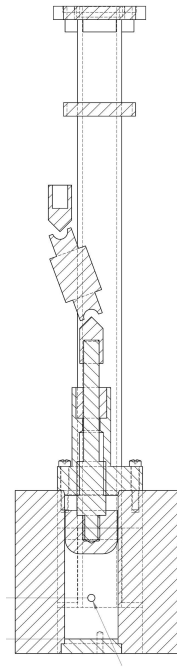


Figure 3: Cross section showing the signal cavity, the plunger with bellows for tuning, and the 2 WR28 waveguides oriented vertically. The circle inside the outline of the cavity denotes the weakly coupled port. Also shown are the threaded fittings and the connector that interfaces with the fiberglass G10 rod.

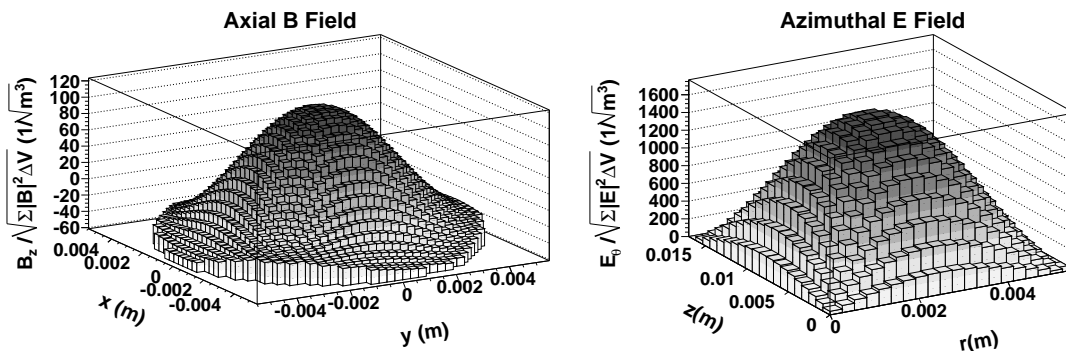


Figure 4: Two important components of the fields in the TE_{011} cavity. The left panel shows B_z , the critical component in Equation 3. The right panel depicts E_θ which is the field that enters into the numerator of Equation 1.

21.1 GHz. It terminates at a waveguide to coax adapter and cryogenic amplifier. The power loss in the waveguide at frequency 34 GHz is acceptable at approximately 1 dB/m. In addition to the critically coupled port, the signal cavity is weakly coupled to 3 m of WR28 waveguide that ends outside the cryostat at a directional coupler. The directional coupler serves two purposes simultaneously: It allows for vacuum pumping and it is a port for test signals. The orientation of the WR28 waveguides relative to the signal cavity are shown in Figure 2.

Inside the signal cavity, two components of the electric and magnetic fields are important in this experiment. The first is the field aligned with the external B-field in the \mathbf{z} direction, which in the case of the TE_{011} mode is theoretically $B_z = k_r/kJ_0(k_r r)\sin(k_z z)$ while $E_z = 0$. In practice B_z is perturbed by its coupling to the waveguide. Its magnitude in the cavity is simulated in accordance with the actual geometry using the HFSS simulation software in ANSYS[®] Academic Research Release 12.1.2 and is plotted in the left panel of Figure 4. In the second signal cavity [28] supporting the TM_{020} mode, $B_z = 0$; the diameter is 15 mm and the height is 9 mm. The axially-aligned electric field takes the analytic form $E_z = k_r/kJ_0(k_r r)$ and is not plotted.

The second important field component to consider is the azimuthal electric field, or $E_\theta = J'_0(k_r r)\sin(k_z z)$. It is the only non-zero component of the electric field in the cylindrical TE_{011} mode. The right panel of Figure 4 shows its analytical form as a function of height and radius in an ideal cavity.

2.2.2. Drive Cavity

The drive cavity runs in the TE_{011} mode at the same resonant frequency as the TE_{011} signal cavity, at room temperature. Like the signal cavity its inner volume is on the order of 1 cm^3 , with diameter 12 mm and height 17 mm. It is typically driven by a narrow monoenergetic signal with $\lesssim 1$ Watt average power which allows for thermal equilibrium without cooling. While its resonant frequency can in principle be tuned by temperature adjustment using water circulation, it is generally more practical to wait for the drive cavity to reach thermal equilibrium and then tune the signal cavity such that their frequencies match.

2.2.3. Field Overlap Integrals

The sensitivity of the experiment to new physics is governed partly by the orientation of the electric and magnetic fields inside the resonant cavity. Each of the two running modes, and each of the two signal cavities, has a field overlap integral that defines its particular ability to detect signals driven by interactions with new light particles.

The running mode with two TE_{011} cavities side by side is optimized to find oscillations between hidden sector photons and Standard Model photons. The sensitivity of the result depends on the overlap integral in [20]

$$G \equiv \omega_o^2 \int_{V'} \int_V d^3\mathbf{x} d^3\mathbf{y} \frac{\exp(ik|\mathbf{x} - \mathbf{y}|)A(\mathbf{y})A'(\mathbf{x})}{4\pi|\mathbf{x} - \mathbf{y}|} \quad (1)$$

where ω_o is the drive frequency and k is the wavenumber of the hidden sector photon. Following the steps in [20] $E = -dA/dt$. Taking the spatial part of $E_\theta(\mathbf{x}, t)$ in the TE_{011} cavities from the right panel of Figure 4, $|G|$ is computed numerically for the two side-by-side cavities in this experiment. Figure 5 shows the result.

Alternatively, in the case of the listening mode that utilizes just one signal cavity, the overlap integral C_{lmn} is defined with respect to the direction of the strong external magnetic field $\hat{\mathbf{B}}$. It is first described in [23, 24] to quantify the response of a resonant cavity to a pseudoscalar axion in a strong magnetic field:

$$C_{lmn} \equiv \frac{\left| \int_V d^3x \mathbf{E} \cdot \hat{\mathbf{B}} \right|^2}{V \int_V d^3x \epsilon_r |\mathbf{E}|^2}, \quad (2)$$

where \mathbf{E} is the electric field in the cavity and V is the volume. In the case

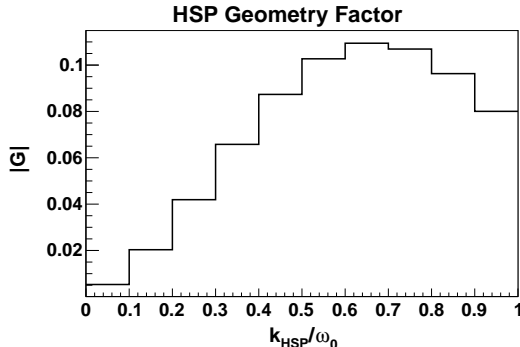


Figure 5: Plot of the field overlap integral for hidden sector photons (HSP), $|G|$ [20], against the wavenumber k_{HSP} .

of the TM_{020} cavity employed in this experiment, C_{lmn} is on the order of 0.1 [28].

For the signal cavity that runs in the TE_{011} mode, C_{lmn} is identically zero because $E_z=0$. However there is a small overlap C'_{lmn} in the case of scalar axion-like particles, adapting the calculation from Eq. 2 as

$$C'_{lmn} \equiv \frac{\left| \int_V d^3x \mathbf{B} \cdot \hat{\mathbf{B}} \right|^2}{V \int_V d^3x \frac{1}{\mu_r} |\mathbf{B}|^2}. \quad (3)$$

The overlap is small at $O(10^{-6})$ because of the behavior of the Bessel function $J_0(k_r r)$ in the axial magnetic field, plotted on the left in Figure 4. The field is positive near the center of the cavity, and negative toward the outer rim. When integrated over the cylindrical volume, $\mathbf{B} \cdot \hat{\mathbf{B}}$ decreases.

2.3. Receiver

2.3.1. Cryogenic amplifier

The first and most critical component in the receiver chain is a low-noise, broadband, high-electron-mobility transistor (HEMT) amplifier [29]. It typically operates at frequencies of 11–26 GHz but is routinely tested for use up to 40 GHz. In this experiment the HEMT is cooled to 7 K and measures broadband noise near 34 GHz. Its specified noise temperature measured at 22 K is approximately 35 K. In Section 3.1 the noise temperature of the HEMT is found to be near 20 K when it is cooled to 7 K. While there are actually two HEMT amplifiers connected in series inside the cryostat for

adequate gain, it is the first HEMT that dictates the noise temperature of the system. The latter remains true as long as its output power is large compared to the noise temperature of the next amplifier.

2.3.2. Room-Temperature electronics

The room-temperature receiver uses a triple heterodyne technique to mix the RF signal down from 34 GHz to baseband. The block diagram is included in Figure 2. The three-stage design has been chosen to avoid possible problems with crosstalk related to high amplification at 34 GHz. Broadband noise is limited at each stage by bandpass filters placed before and after the amplifiers, thereby avoiding saturation.

Power at the image frequencies is suppressed by more than 100 dB with the bandpass filters (BPFs) that sit before the first two mixers. For example, if RF frequency f_1 mixes with LO frequency f_2 , then the intermediate frequency (IF) is $f_1 - f_2$ and the image lies at $2f_2 - f_1$. It is this image frequency that must lie outside the passband of the BPF that precedes each mixer. If it were not suppressed then the noise power would increase by a factor of 2 after the mixer. In the case of the third mixer, a different technique is used to suppress the image power. The outputs of the mixer in the baseband are separated into the in-phase (I) and quadrature (Q) voltages. The image power in the baseband is suppressed by selecting the sign of the complex phase $\phi = \tan^{-1}(Q/I)$.

The first six harmonics of each LO are also excluded from the passband of the receiver. For example, the second LO in the chain oscillates at 3.5 GHz, so its first 6 harmonics are 7.0 GHz, 10.5 GHz, 14.0 GHz, 17.5 GHz, 21.0 GHz, and 24.5 GHz. The frequency plan is chosen so that these harmonics do not propagate through the electronics chain into the baseband. If a harmonic did pass into the baseband, it could mimic a real signal and cause difficulty in the offline analysis. In spite of the above it should be noted that harmonics with even higher orders are still expected to be present in the data; care is required, as always, in discriminating between a real signal and a systematic or environmental feature.

As a preliminary check of the receiver's performance, the output of the room temperature chain has been checked against its specifications at the first two stages with a 50 Ω termination at the input. The specified noise figure and gain of the components in the room-temperature chain are cascaded

component	measured (dBm/Hz)	predicted (dBm/Hz)
300K 50Ω term.	<-150	-174
mixer 1	<-150	-173
IF1 amp	-112	-112
mixer 2	-116	-118
IF2 amp	-85	-85

Table 1: Table of noise power measured after the first two stages of the microwave receiver, compared with values expected from the Friis formula for cascaded noise power.

according to the Friis formula for total noise factor

$$F = F_1 + \frac{F_2 - 1}{G_1} + \frac{F_3 - 1}{G_1 G_2} + \dots, \quad (4)$$

where F represents the total noise factor, F_i is the specified noise factor for component i , and G_i is the gain of component i . The expected noise power in the chain at any given point i is $N_S + G + 10\log_{10}(F)$ dBm/Hz where N_S is the noise power of the source at the input to the chain and G is the total gain. The predicted noise power is then compared with the measured noise power in Table 1, with reasonable agreement.

As shown in Figure 2, a low-pass filter typically precedes the digitizer in each of the two paths I and Q . Figure 6 shows the baseband power in I and Q measured with an Agilent PXA N9030 spectrum analyzer (left panel) and with the digitizer (right panel). The absolute magnitudes derived from each instrument are not expected to be identical due to losses that are characteristic of each digitizer. However the relative magnitudes of the power in I and Q are expected to match.

3. Measurements

3.1. Noise Calibration

The system noise temperature T_{sys} is the figure of merit that drives the statistical uncertainty σ_T in the measurements, according to the Dicke radiometer equation [30]

$$\sigma_T = \frac{T_{sys}}{\sqrt{\Delta\nu\tau}} \quad (5)$$

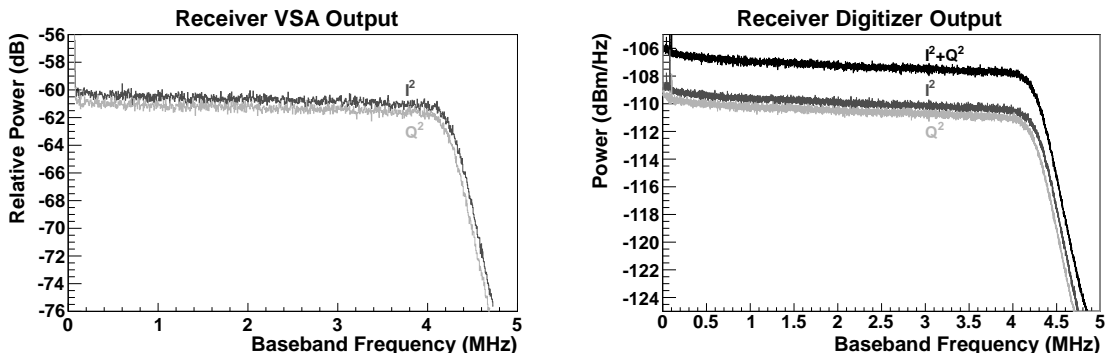


Figure 6: Plots comparing the output of the receiver chain in the baseband. The left panel shows the outputs in I and Q measured with the spectrum analyzer. The right panel shows the outputs after the digitizer and offline analysis.

where $\Delta\nu$ is the resolution bandwidth and τ is the integration time. From the equation, σ_T decreases with longer integration times and increases with narrower bandwidths. In this experiment, $T_{sys} = T_{\text{HEMT}} + T_{th}$, where T_{HEMT} is the noise temperature of the HEMT and T_{th} is the physical temperature of the HEMT's chassis and connectors.

The total uncertainty σ_{tot} in the measurements is driven by both the statistical uncertainty σ_T and the systematic uncertainties σ_{sys} . Effectively the two sources of error are combined in quadrature as

$$\sigma_{tot} = \sqrt{\sigma_T^2 + \sigma_{sys}^2}. \quad (6)$$

From Equation 6, σ_{tot} improves with integration time only until $\sigma_T < \sigma_{sys}$. This means that in a system with high T_{sys} and small $\Delta\nu$, long integration times (\sim hours) can be beneficial. Conversely, for low T_{sys} and large $\Delta\nu$, the condition $\sigma_T < \sigma_{sys}$ happens quickly and σ_{tot} may be optimal after relatively short integration times (\sim seconds).

3.1.1. Noise power density and twice power methods

The system noise temperature is measured using several approaches, and the results are compared. First is a measurement of the total output noise power with a matched 50Ω terminator at the input to the cold HEMT. In this approach, the mean output power divided by the gain of the electronics chain is defined as T_{sys} . For this purpose the gain of the electronics chain is measured with a test signal that is sent through the electronics chain by

way of the calibration waveguide. However, a problem with this technique is that the power contained in the test signal is reduced by the line loss, or the loss in the waveguide and through both ports in the cavity at cryogenic temperatures. Because these behaviors are hard to characterize in the presence of reflections and standing waves, the gain inferred from a test signal is reported only as a function of the line loss. Figure 7 shows an example of a test signal sitting on a background of amplified thermal and electronic noise.

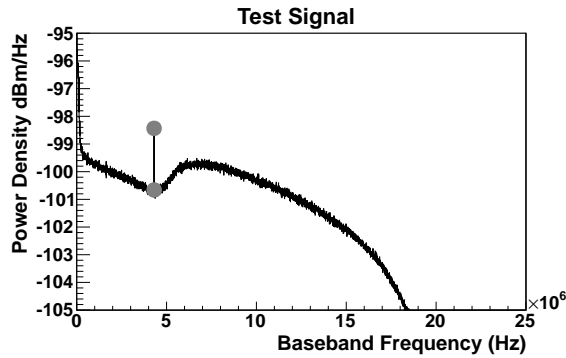


Figure 7: Broadband noise measured in the baseband without the low pass filters in place. The spike at 4 MHz is a test signal that was sent into the cavity through the weakly coupled calibration port.

With the gain defined as above, T_{sys} can be derived as a function of the line loss. With a $50\ \Omega$ termination at the input to the 7 K HEMT, the output power is corrected for the hardware transfer function and divided by an array of values for the gain. An example for one value of the gain is shown on the left in Figure 8, and the results for the other gains are included on the right in Figure 9.

The noise factor of the electronics, driven by T_{HEMT} , can also be deduced with the “twice-power” method. In this approach a narrow test signal with power P_{in} is injected into the electronics until it sits $2\times$ higher than than the baseline noise at the output of the electronics. Then, the noise factor $F \equiv P_{in}/k_B T \Delta\nu$ where $k_B T \Delta\nu$ is the baseline noise at the input. Both P_{in} and $k_B T \Delta\nu$ are extracted using the gain of the electronics chain, which as stated above, is still a theoretical function of the line loss. On the right in Figure 8 is a plot of P_{out} against P_{in} for a set of test signals with a range of magnitudes. The condition $P_{in}/P_{baseline} \equiv 2$ is determined by interpolation

in order to calculate F . The noise factor and noise temperature T of the HEMT are related as $T = (F - 1)T_0$ where T_0 is the temperature of the HEMT's chassis. T_{sys} is then derived by adding the chassis temperature T_{th} to T . The right panel of Figure 9 includes T_{sys} derived from F as a function of the line loss. As shown on the plot, the results agree well with T_{sys} taken from the measurements of the mean broadband noise from the matched $50\ \Omega$ termination.

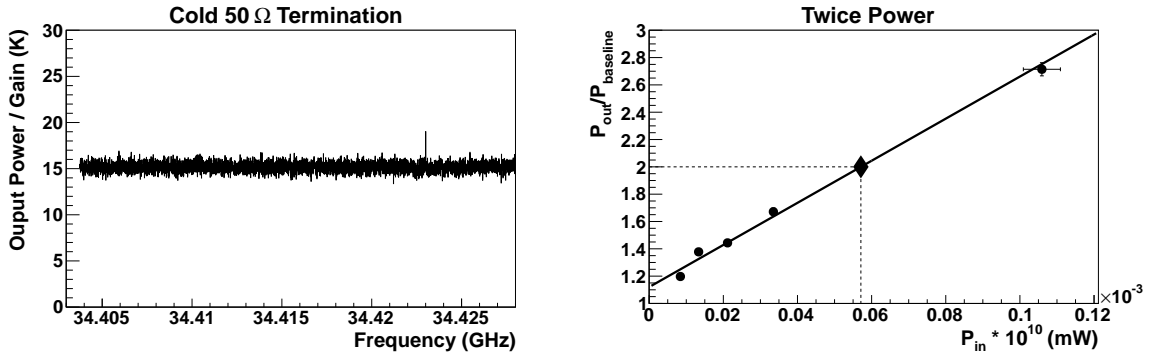


Figure 8: The left panel shows broadband noise from the receiver, corrected for the hardware transfer function, with a 7 K matched $50\ \Omega$ termination at the input. The spike at 34.423 GHz is related to the 10 MHz reference oscillator. The circular points in the right panel show the magnitudes of a series of test signals relative to the surrounding noise, plotted against the presumed input power P_{in} . The input power for which the output power is doubled is inferred by interpolation, shown as the diamond marker on the plot. The magnitudes of P_{in} have been temporarily scaled by a factor of 10^{10} to accommodate the precision of the fitting algorithm on the 32-bit computer.

3.1.2. Y-Factor Method

The uncertainty caused by the line loss described in the previous section is removed with a Y-factor measurement. In this approach, the frequency-dependent noise temperature of the amplifier is derived from the ratio of two spectra with different input temperatures while the temperature of the HEMT is held constant. The first spectrum is taken using a cold source (~ 7 K) as the input, and the second with a warm source (~ 28 K). The temperature of the HEMT is reasonably constant, ranging between 4.5 and 8 K. The temperatures are determined with the thin-film resistance cryogenic temperature sensors. The noise temperature of the amplifier is defined as the X-intercept on a graph of output power plotted against source temperature. The data are collected using an Agilent 9030A spectrum analyzer.

During the measurement, a Cu block is in thermal contact with a $50\ \Omega$ termination that is connected to the input of the HEMT using a 5 cm long 0.085" diameter cable with stainless steel jacket, PTFE dielectric interior, and stainless steel inner conductor. The cable provides some thermal isolation between the HEMT and the termination. Additional isolation is achieved by wrapping the block loosely with mylar lined on the inside with a layer of Dacron mesh. For temperature stability, the HEMT is thermally coupled to a pool of liquid He at the bottom of the cryostat with an OFHC Cu cold finger. The temperature of the source is increased by applying current to a resistor that is in thermal contact with the Cu block.

Figure 9 summarizes the results of the Y-factor measurement. The left panel contains the extracted noise temperature of the electronics, driven by the HEMT. The largest sources of uncertainty come from imperfect thermal contact between the temperature sensors and the warm and cold terminations, and from unwanted heating of the amplifier during the measurement. Additional errors arise from a lack of thermal equilibrium between the Cu block and the $50\ \Omega$ termination, time lag between heating of the source and the data collection, and uncertainty in the amount of RF power lost in the stainless steel cable. The loss in the stainless steel cable is estimated to be 0.6 dB, adjusted downward from 0.9 dB at room temperature according to the expected lowering of electrical resistivity at 5 K [31]. Considering all of the above, T_{HEMT} is probably near 20 ± 5 K. The right panel of Figure 9 shows $T_{\text{sys}} = T_{\text{HEMT}} + T_{\text{th}} \cong 27\pm 5$ K taken from the Y-factor measurement, plotted simultaneously with the measurements discussed in Section 3.1.1. As a result of the Y-factor measurement the gain of the system is inferred to be 84.0 ± 1.0 dB.

The measured noise temperature of the amplifier falls within a factor of 12 ± 3 of the standard quantum limit at 34 GHz $hf/k_B = 1.6$ K. While this is not atypical for a HEMT amplifier whose semiconductor structures are built from InP [32], it is perhaps notable that the noise performance does not appear to be significantly degraded by the strong 7 T magnetic field. Daw and Bradley [33] found that the noise performance of a HEMT built with GaAs/AlGaAs and operating at 683 MHz was degraded by the presence of an ambient 3.6 T magnetic field. The effect was found to be highly dependent on the orientation of the amplifier relative to the field. A quantitative account for the behaviors was given in terms of the electrons' trajectories across the two-dimensional electron gas between semiconductor layers [33].

For the case of the InP HEMT in the present experiment, there is no

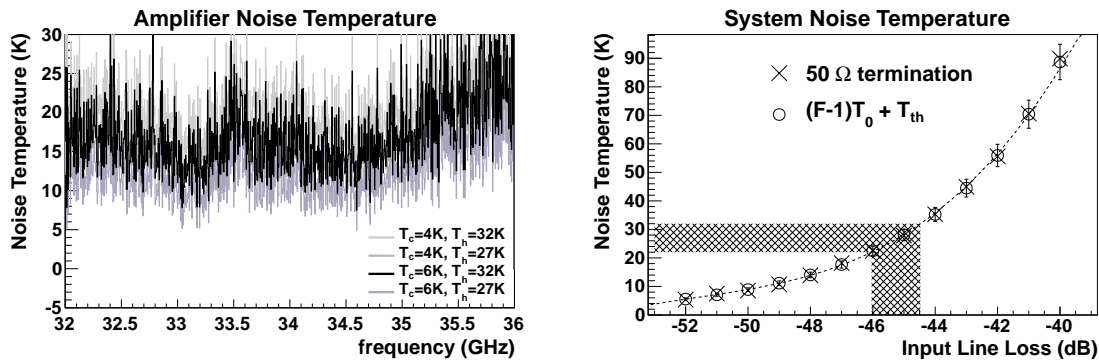


Figure 9: The left panel shows the amplifier noise temperature derived from the Y-factor measurement. The legend contains several sets of plausible cold and warm source temperatures T_c and T_h . In the right panel, the shaded region shows T_{sys} inferred from the left panel assuming a cryostat temperature T_{th} of 7 K. The right panel also depicts T_{sys} as calculated from measurements with a 50Ω termination and from the twice-power method.

obvious reason why the electrons in the two-dimensional gas should not be affected by the magnetic field similarly to [33]. Furthermore, through engineering constraints the amplifier is oriented relative to the magnetic field such that if there is such an effect, it should be maximal. Additional investigation is therefore required to fully characterize the noise performance of the InP HEMT in the magnetic field, including observations of the current drawn, the gain, and the inferred noise temperature.

As a complement to the above measurement of the mean T_{sys} , it is important to examine the distribution of individual power samples. Their values are expected to have a predictable behavior when sampled with an ideal total power radiometer. The raw sampled voltages V should follow a Gaussian distribution in number density centered around 0 V. The power measurements should fall inside the same Gaussian, squared [34]

$$P(V^2) \sim \frac{1}{V} e^{(-V^2)/(2\sigma^2)}, \quad (7)$$

where σ is the standard deviation of the Gaussian and σ^2 becomes the mean of the Gaussian squared [34]. Applying the envelope $P(V^2)$ to a random number generator simulates the output of an ideal radiometer. Figure 10 shows a plot of the simulated data compared with real data from this experiment. The means in each distribution are the same. From the plot it is apparent that the qualitative behavior of the two data sets are similar. Differences are also

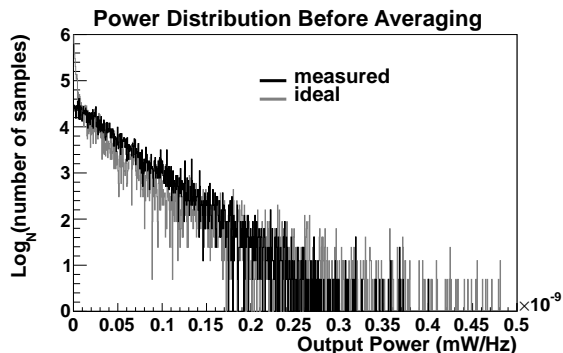


Figure 10: Distribution of power measured with the receiver, plotted simultaneously with the ideal distribution having the same mean.

present: The ideal data contain samples at the low and high energies that are not present in the real data. These are attributed to the finite noise floor of the digitizer on the low end, and to infrequent saturation of the receiver on the high end. The slight discrepancy near 0.05 mW/Hz is caused by the low energy tail combined with the arbitrary requirement that the mean be identical in both data sets.

3.2. Wave Model

In the previous section the system noise temperature T_{sys} was discussed. In this section T_{sys} will be considered only as it applies to the system with a resonant cavity at the input. Following the approach discussed in [35, 36] for a noisy two-port device coupled to a noise source, a model of the present experiment is constructed. Figure 11 shows a block diagram of the cavity, WR28-to-coaxial adapter, and the HEMT amplifier with the noise fields and their directions. As in [35] A_n and B_n are the complex ingoing and outgoing noise waves of the amplifier. A_{th} , A_{ad} , and A_{cav} are the waves associated with the physical temperatures of the 3 components, where $|A_{th}| > |A_{ad}| > |A_{cav}|$. The reflection and transmission coefficients Γ and τ are determined from the return loss (RL) such that $RL(\text{dB}) = -20\log_{10}(|\Gamma|)$ and $|\Gamma|^2 + |\tau|^2 \equiv 1$. L_1 and L_2 are electrical lengths.

Summing the fields at the input to the HEMT gives

$$A_n + A_{th} + \Gamma_1 B_n + A_{ad} + \tau_1(A_{cav} + \Gamma_2(B_n \tau_1 + A_{ad})),$$

which reduces to $A_n + A_{th} + \Gamma_1 B_n + \tau_1^2 \Gamma_2 B_n$ because the HEMT is warmer than the adapter and the cavity. The power at the input to the HEMT

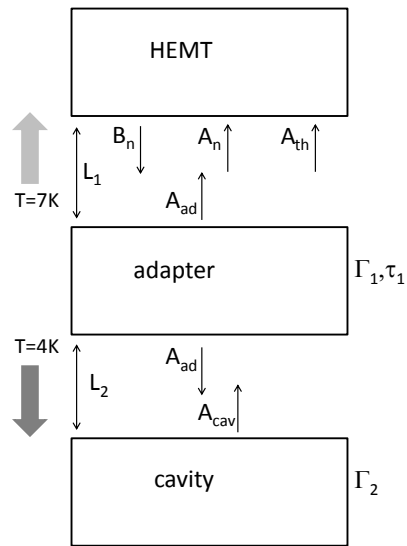


Figure 11: Block diagram as the basis for a wave model of the noise properties of the experiment, after [35]. L_1 and L_2 are electrical lengths, and Γ and τ are reflection and transmission coefficients. The fields A_n and B_n are characteristic of the amplifier. All other fields are derived from physical temperatures.

is taken from the square of the summed fields. Following the steps in [35] which are partially summarized in Equations 8–11, correlated cross terms retain a phase shift and uncorrelated cross terms collapse to zero. The noise temperature of the amplifier is proportional to $|A_n|^2$. The waves A_n and B_n going in and out of the amplifier are correlated by a phase shift ϕ_c . The electrical lengths L_1 and $L_1 + L_2$ behave as phase shifts in the reflection coefficients Γ_1 and Γ_2 .

$$|A_n|^2 = k_B T_a \Delta f \quad (8)$$

$$|B_n|^2 = k_B T_b \Delta f \quad (9)$$

$$A_n * B_n = k_B T_c \Delta f e^{i\phi_c} \quad (10)$$

$$\Gamma = |\Gamma| e^{i\phi_s} \text{ where } \phi_{s1} = 2L_1/\lambda \text{ and } \phi_{s12} = 2(L_1 + L_2)/\lambda. \quad (11)$$

Squaring the fields and collecting the cross terms, the power at the input to the HEMT is expected to be

$$T_a + T_{th} + |\Gamma_1|^2 T_b + |\Gamma_2|^2 T_b |\tau_1|^4 + 2|\Gamma_1| T_c \cos(\phi_{s1} + \phi_c) + 2|\Gamma_2| T_c \tau_1^2 \cos(\phi_{s12} + \phi_c) + 2|\Gamma_2| |\Gamma_1| T_b \tau_1^2 \cos(\phi_{s1} + \phi_{s12}). \quad (12)$$

The first two terms $T_a + T_{th}$ are equivalent to T_{sys} , estimated to be 27 K in Section 3.1. The parameters $|\Gamma_1|$ and $|\Gamma_2|$ are measured at cryogenic temperatures in terms of return loss with the Agilent PNA E8364C network analyzer and are labeled S11 and S22 in Figure 12. Oscillations with frequency 50 MHz can also be seen on the plots. These features indicate the presence of well-behaved reflections inside the 6 m round-trip length of waveguide. The loaded Q of the TE₀₁₁ cavity is measured at 5 K and is labeled S21 in Figure 12. From the S22 of the cavity on resonance (-12 dB) and the measurement of Q at 10^4 , the frequency-dependent Γ_2 behaves as a Lorentzian

$$|\Gamma_2| = \frac{10^{-12./20}}{1 + \left(\frac{2Q(f-f_0)}{f_0}\right)^2}.$$

Remaining parameters that are unmeasured in the model are the three phase shifts ϕ_1 , ϕ_{12} , and ϕ_c , as well as T_b and T_c . The bottom right panel of Figure 12 shows an overlay of the model with the data from the receiver with the 5 K resonant cavity at the input. The free parameters have been adjusted by hand in the plot to be $T_c=3.0$ K, $T_b=0.5$ K, $\phi_c=0$, $\phi_{s1}=0$, and $\phi_{s12}=0$. Although the solution is not a unique one, it is still encouraging that the model can account for the observations made in this experiment.

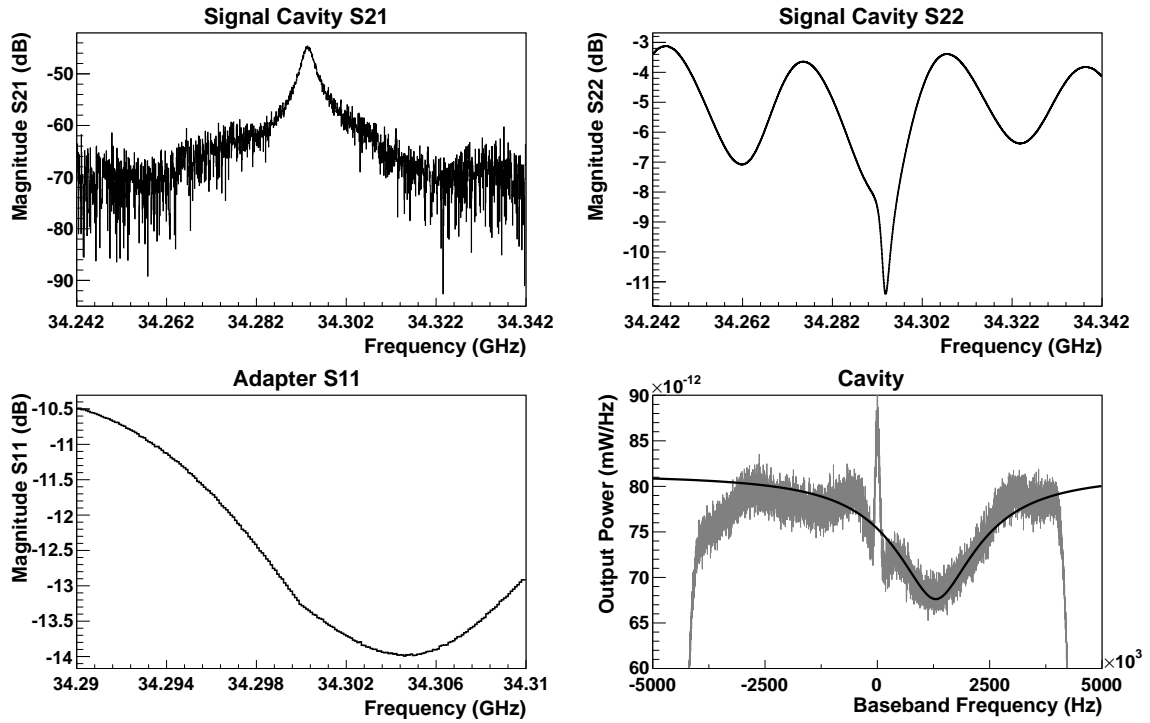


Figure 12: Upper left panel: Transmitted power from which the Q of the TE_{011} cavity is derived. Upper right: Power reflected from the cold TE_{011} cavity tuned to 34.294 GHz. Lower left: Power reflected from the cold waveguide to coaxial adapter. Lower right: Wave model (solid line) from equation 12 incorporating the measurements from the other three panels in this figure.

3.3. Data Reduction

The aim of the data processing is to optimize the signal to noise ratio

$$\frac{S}{N} = \frac{P_{sig}\sqrt{\tau}}{k_B T_{sys}\sqrt{\Delta\nu}} \quad (13)$$

where P_{sig} is the signal power, $k_B\sigma_T\Delta\nu$ is the noise power, and σ_T is defined in Equation 5. The bandwidth of P_{sig} in Equation 13 is assumed to be narrower than $\Delta\nu$. From the expression it is clear that P_{sig} increases as $\sqrt{\tau}$ and as $1/\sqrt{\Delta\nu}$. It is therefore beneficial to choose the narrowest possible value of $\Delta\nu$ while still requiring that it encapsulate the width of P_{sig} .

After selecting the resolution bandwidth, the data are converted from a raw time series of voltages in I and Q to a power spectrum in frequency. This is done using a complex Fast Fourier Transform (FFT) taken from the `fftw3` [37] libraries. After the FFTs there are $N = \tau\Delta\nu$ frequency spectra that are averaged together.

3.4. Driven Experiment

In the case of the two-cavity experiment, the data reduction is a straightforward search for a monoenergetic signal at the same frequency as the drive signal. Also, since the drive signal is narrow (<10 mHz) and is frequency-locked to the receiver chain, $\Delta\nu$ should be narrow to optimize the signal to noise ratio (e.g. [38, 39]).

Figure 13 shows an example of a data run with an RF leak (left panel), and with the RF leak suppressed (right panel). The expected frequency of the drive signal in the baseband is noted with an arrow. In looking at the figure one might notice that the width of the RF leak appears to span more than one bin. At first glance this may be surprising given that the source is narrow, $\Delta\nu$ is 6.7 mHz, and the system is frequency-locked. However in this particular measurement the RF leak was found to be related to a ground loop that included the two cryogenic amplifiers and their power supplies, which probably means that the power in this RF leak was not well locked to the rest of the system. This can account for the excess width in the signal.

The shielding between the two cavities is demonstrated, also in Figure 13. The power contained in the RF leak is 10^{-21} Watts. The signal appears at the expected frequency in the baseband which demonstrates that the detection and analysis are working correctly. With the RF leak suppressed, as in the right panel, the shielding is estimated from the drive power and σ_{tot} to be $P_{sig}/(k_B\sigma_{tot}\Delta\nu) \geq 223$ dB.

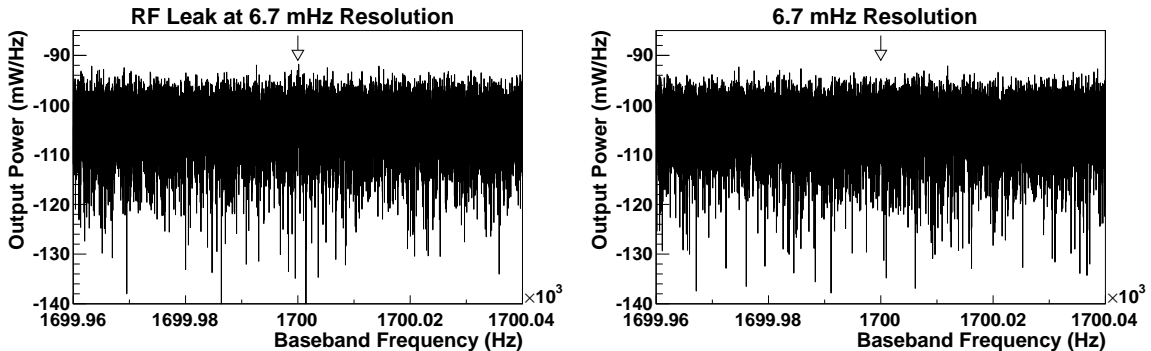


Figure 13: The left panel shows the power from the signal cavity in the presence of an RF leak. The right panel shows the power spectrum without the RF leak. The arrow in each plot marks the frequency in the baseband where the drive signal should be after downmixing.

3.5. Listening Experiment

In the swept search for halo ALPs with one cavity, the data analysis begins with the FFT as above in the driven experiment. Following the FFT are several additional steps that are needed to account for the interaction of the ALP-driven photons with the apparatus. These steps are more critical here than they are in the driven experiment largely because the frequency of the signal is unknown. Thus it becomes important to characterize each bin for every cavity frequency before averaging the overlapping scans. The steps outlined here are similar to those described in [25] and [40]. To date the analysis has been focused on a search for statistical aberrations that are one bin wide, using a resolution bandwidth of 34 kHz across a tuning bandwidth of 600 MHz. Wider scan ranges are possible but are probably best approached with an automated experiment.

3.5.1. Mean subtraction

The first step in the analysis after the FFT is to extract the raw fluctuations from around the mean power. To do this, the mean is calculated empirically and is subtracted from the power spectrum. Typically the mean is derived from the data in groups of ~ 5 bins at a time; this ensures accuracy without significant degradation of narrow signals.

3.5.2. Mismatch

The impedance mismatch between the cavity and the waveguide acts as a filter during the measurement. For the case of a cavity critically coupled to the waveguide on resonance, half of the power in the cavity propagates to the waveguide. Off resonance, less than half of the power propagates. The function describing this behavior in frequency is a Lorentzian curve with the Q of the cavity, peaking at 0.5. It is applied to the fluctuations by division, which worsens the resolution everywhere by at least a factor of 2. The coupling of the TM_{020} cavity to the waveguide has been measured to be close to critical in [28]. For the case of a cavity with some other degree of coupling, the mismatch filter is derived similarly but with a different peak value that corresponds to the fraction of power transmitted out of the cavity on resonance.

3.5.3. Noise reduction filter

The narrow signal that is expected from ALP couplings coexists with the random thermal and electronic noise characterized by T_{sys} . Therefore the signal to noise ratio is improved by an algorithm that reduces the random noise power. The Wiener filter [41] is one example of a useful and accessible tool for this purpose, implemented as in [42]

$$b_i = \mu + \frac{(\sigma^2 - \nu^2)}{\sigma^2}(a_i - \mu)$$

where a_i (b_i) is the unfiltered (filtered) fluctuation in bin i , σ is the standard deviation in the neighborhood of bin i , ν is the average value of σ near bin i , and μ is the mean of a_i near bin i . The typical granularity of the filter in this analysis is about 10 bins.

3.5.4. Axion Lorentzian

The last step is to consider the power spectrum of photons that should come from axion couplings within the volume of the resonant cavity. The power P_0 for the case where the axion mass is equal to the resonant frequency of the cavity is calculated from the Lagrangian in [23, 24]. Where the mass is off resonance, the power spectrum is also derived from the Lagrangian and follows the Lorentzian shape of the cavity resonance [23, 24, 43]. In practice this behavior is applied to the data in frequency as a division by a Lorentzian function that peaks at unity. Figure 14 shows a typical data set measured in the listening mode with the TM_{020} cavity, before and after the data reduction.

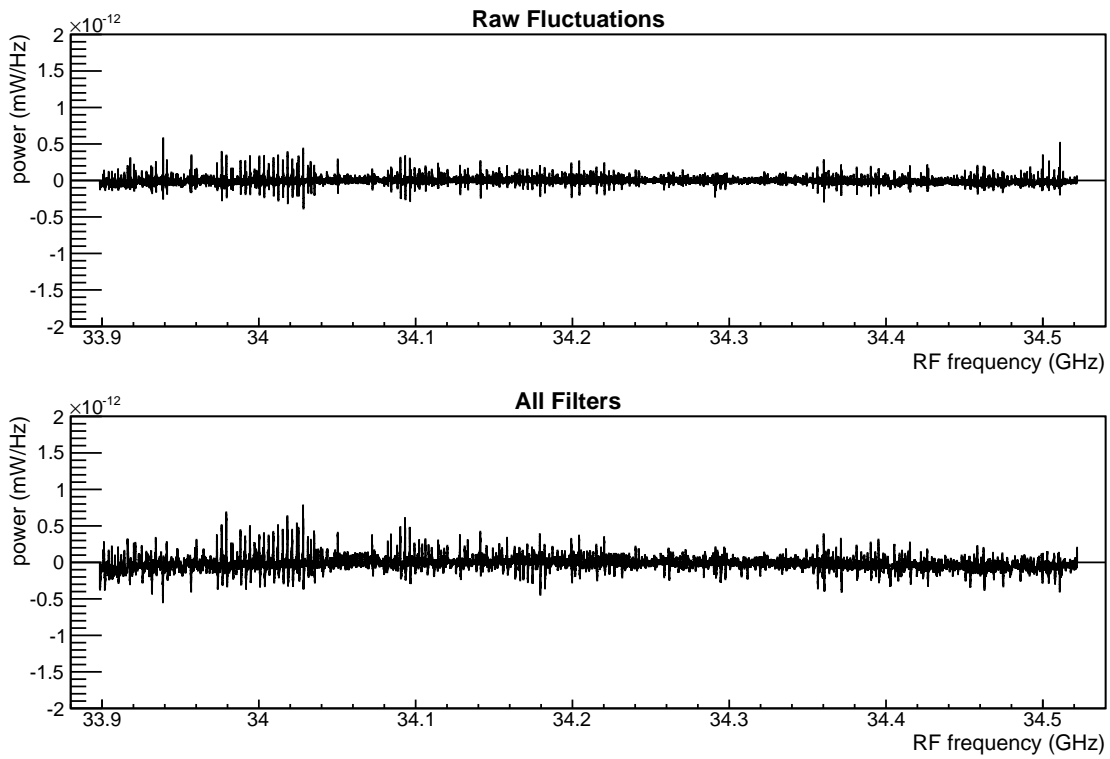


Figure 14: Two plots showing a sample of raw fluctuations in the data before (top panel) and after (bottom panel) the data reduction in the listening experiment, using with one cavity in the TM_{020} mode. The resolution bandwidth is 34 kHz.

4. Summary

The design and nominal behavior of the Yale 34 GHz resonant cavity experiment has been described. The noise temperature of the electronics has been measured. The observations made with the apparatus have been compared with expected values, and the data reduction has been outlined. The measurements and their derivation are in accordance both with ideal models and with techniques used in other experiments [23, 27]. It is therefore reasonable to conclude that if an unexpected signal were to be found in this experiment it should be investigated as a possible sign of new physics.

5. Acknowledgments

The authors are grateful to the United States Office of Naval Research Directed Energy Program and to Yale University for their generous financial support. The authors also wish to thank Professor Kurt Zilm for the use of the NMR magnet throughout this experiment.

References

- [1] F. Zwicky, On the Masses of Nebulae and of Clusters of Nebulae, *Astrophys.J.* 86 (1937) 217–246. doi:10.1086/143864.
- [2] Y. Sofue, M. Honma, T. Omodaka, Unified Rotation Curve of the Galaxy – Decomposition into de Vaucouleurs Bulge, Disk, Dark Halo, and the 9-kpc Rotation Dip –, *Publ.Astron.Soc.Japan* 61 (2009) 227–236. arXiv:0811.0859.
- [3] N. Jarosik, C. Bennett, J. Dunkley, B. Gold, M. Greason, et al., Seven-Year Wilkinson Microwave Anisotropy Probe (WMAP) Observations: Sky Maps, Systematic Errors, and Basic Results, *Astrophys.J.Suppl.* 192 (2011) 14. arXiv:1001.4744, doi:10.1088/0067-0049/192/2/14.
- [4] Tauber, Jan, Planck 2013 results. i. overview of products and scientific results, *A&A* doi:10.1051/0004-6361/201321529. URL <http://dx.doi.org/10.1051/0004-6361/201321529>
- [5] C. Aalseth, et al., CoGeNT: A Search for Low-Mass Dark Matter using p-type Point Contact Germanium Detectors, *Phys.Rev. D* 88 (1) (2013) 012002. arXiv:1208.5737, doi:10.1103/PhysRevD.88.012002.

- [6] G. Angloher, M. Bauer, I. Bavykina, A. Bento, C. Bucci, et al., Results from 730 kg days of the CRESST-II Dark Matter Search, *Eur.Phys.J. C* 72 (2012) 1971. [arXiv:1109.0702](#), [doi:10.1140/epjc/s10052-012-1971-8](#).
- [7] R. Bernabei, et al., First results from DAMA/LIBRA and the combined results with DAMA/NaI, *Eur.Phys.J. C* 56 (2008) 333–355. [arXiv:0804.2741](#), [doi:10.1140/epjc/s10052-008-0662-y](#).
- [8] C. Savage, G. Gelmini, P. Gondolo, K. Freese, Compatibility of DAMA/LIBRA dark matter detection with other searches, *JCAP* 0904 (2009) 010. [arXiv:0808.3607](#), [doi:10.1088/1475-7516/2009/04/010](#).
- [9] R. Agnese, et al., Silicon Detector Dark Matter Results from the Final Exposure of CDMS II, *Phys.Rev.Lett.* 111 (2013) 251301. [arXiv:1304.4279](#), [doi:10.1103/PhysRevLett.111.251301](#).
- [10] E. Aprile, et al., Limits on spin-dependent WIMP-nucleon cross sections from 225 live days of XENON100 data, *Phys.Rev.Lett.* 111 (2) (2013) 021301. [arXiv:1301.6620](#), [doi:10.1103/PhysRevLett.111.021301](#).
- [11] J. Angle, et al., A search for light dark matter in XENON10 data, *Phys.Rev.Lett.* 107 (2011) 051301. [arXiv:1104.3088](#), [doi:10.1103/PhysRevLett.110.249901](#), [10.1103/PhysRevLett.107.051301](#).
- [12] E. Armengaud, et al., Final results of the EDELWEISS-II WIMP search using a 4-kg array of cryogenic germanium detectors with interleaved electrodes, *Phys.Lett. B* 702 (2011) 329–335. [arXiv:1103.4070](#), [doi:10.1016/j.physletb.2011.07.034](#).
- [13] E. Armengaud, et al., A search for low-mass WIMPs with EDELWEISS-II heat-and-ionization detectors, *Phys.Rev. D* 86 (2012) 051701. [arXiv:1207.1815](#), [doi:10.1103/PhysRevD.86.051701](#).
- [14] D. Y. Akimov, H. Araujo, E. Barnes, V. Belov, A. Bewick, et al., WIMP-nucleon cross-section results from the second science run of ZEPLIN-III, *Phys.Lett. B* 709 (2012) 14–20. [arXiv:1110.4769](#), [doi:10.1016/j.physletb.2012.01.064](#).

- [15] D. Akerib, et al., First results from the LUX dark matter experiment at the Sanford Underground Research Facility, *Phys.Rev.Lett.* 112 (2014) 091303. [arXiv:1310.8214](#), [doi:10.1103/PhysRevLett.112.091303](#).
- [16] G. Aad, et al., Search for dark matter candidates and large extra dimensions in events with a jet and missing transverse momentum with the ATLAS detector, *JHEP* 1304 (2013) 075. [arXiv:1210.4491](#), [doi:10.1007/JHEP04\(2013\)075](#).
- [17] R. Peccei, H. R. Quinn, CP Conservation in the Presence of Instantons, *Phys.Rev.Lett.* 38 (1977) 1440–1443. [doi:10.1103/PhysRevLett.38.1440](#).
- [18] S. Weinberg, A New Light Boson?, *Phys.Rev.Lett.* 40 (1978) 223–226. [doi:10.1103/PhysRevLett.40.223](#).
- [19] F. Wilczek, Problem of Strong p and t Invariance in the Presence of Instantons, *Phys.Rev.Lett.* 40 (1978) 279–282. [doi:10.1103/PhysRevLett.40.279](#).
- [20] J. Jaeckel, A. Ringwald, A Cavity Experiment to Search for Hidden Sector Photons, *Phys.Lett.* B659 (2008) 509–514. [arXiv:0707.2063](#), [doi:10.1016/j.physletb.2007.11.071](#).
- [21] P. Arias, D. Cadamuro, M. Goodsell, J. Jaeckel, J. Redondo, et al., WISPy Cold Dark Matter, DESY-11-226, MPP-2011-140, CERN-PH-TH-2011-323, IPPP-11-80, DCPT-11-160 [arXiv:1201.5902](#).
- [22] A. E. Nelson, J. Scholtz, Dark Light, Dark Matter and the Misalignment Mechanism, *Phys.Rev.* D84 (2011) 103501. [arXiv:1105.2812](#), [doi:10.1103/PhysRevD.84.103501](#).
- [23] P. Sikivie, Experimental Tests of the Invisible Axion, *Phys.Rev.Lett.* 51 (1983) 1415–1417. [doi:10.1103/PhysRevLett.51.1415](#).
- [24] P. Sikivie, Detection rates for 'invisible' axion searches, *Phys. Rev.* D32 (1985) 2988. [doi:10.1103/PhysRevD.36.974](#), [10.1103/PhysRevD.32.2988](#).
- [25] H. Peng, S. J. Asztalos, E. Daw, N. Golubev, C. Hagmann, et al., Cryogenic cavity detector for a large scale cold dark-matter axion

- search, Nucl.Instrum.Meth. A444 (2000) 569–583. doi:10.1016/S0168-9002(99)00971-7.
- [26] R. Bradley, J. Clarke, D. Kinion, L. Rosenberg, K. van Bibber, et al., Microwave cavity searches for dark-matter axions, Rev. Mod. Phys. 75 (2003) 777–817. doi:10.1103/RevModPhys.75.777.
- [27] S. Asztalos, et al., A SQUID-based microwave cavity search for dark-matter axions, Phys.Rev.Lett. 104 (2010) 041301. arXiv:0910.5914, doi:10.1103/PhysRevLett.104.041301.
- [28] A. T. Malagon, Search for 140 μeV Pseudoscalar and Vector Dark Matter Using Microwave Cavities, Ph.D. Thesis, Yale University (2014).
- [29] S. Weinreb, M. W. Pospieszalski, R. Norrod, Cryogenic HEMT Low-Noise Receivers for 1.3 to 43 GHz Range, Microwave Symposium Digest, 1988., IEEE MTT-S International 2 (1988) 945–948. doi:10.1109/MWSYM.1988.22187.
- [30] R. H. Dicke, Rev. Sci Instrum. 17 (1946) 268.
- [31] J. G. Hust, P. J. Giarratano, Standard Reference Materials: Thermal Conductivity and Electrical Resistivity. Standard Reference Materials: Austenitic Stainless Steel, SRMs 735 and 798, From 4 to 1200 K., Nat. Bur. Stand. (U.S.) Spec. Publ. 260-46, Washington, D.C., 1975.
- [32] M. Reid, Low-noise systems in the Deep Space Network, Wiley, Hoboken, N.J, 2008.
- [33] E. Daw, R. F. Bradley, Effect of High Magnetic Fields on the Noise Temperature of a Heterostructure Field-Effect Transistor Low-Noise Amplifier, J.Appl.Phys. 82 (1997) 1925. doi:10.1063/1.366000.
- [34] J. J. Condon, S. M. Ransom, Essential radio astronomy.
URL www.cv.nrao.edu/course/astr534/ERA.shtml
- [35] R. P. Meys, A wave approach to the noise properties of linear microwave devices, IEEE Trans. on Microwave Theory and Tech. 26 (1) (1978) 34–37.

- [36] S. W. Wedge, D. B. Rutledge, Wave Techniques for Noise Modeling and Measurement, *IEEE Trans. on Microwave Theory and Tech.* 40 (11) (1992) 2004–2013.
- [37] M. Frigo, S. G. Johnson, The design and implementation of FFTW3, *Proc. IEEE* 93 (2005) 216–231. doi:10.1109/JPROC.2004.840301.
- [38] F. Caspers, J. Jaeckel, A. Ringwald, Feasibility, engineering aspects and physics reach of microwave cavity experiments searching for hidden photons and axions, *JINST* 4 (2009) P11013. arXiv:0908.0759, doi:10.1088/1748-0221/4/11/P11013.
- [39] M. Betz, F. Caspers, M. Gasiot, M. Thumm, S. Rieger, First results of the CERN Resonant Weakly Interacting sub-eV Particle Search (CROWS), *Phys.Rev. D* 88 (7) (2013) 075014. arXiv:1310.8098, doi:10.1103/PhysRevD.88.075014.
- [40] E. J. Daw, A search for halo axions, Ph.D. Thesis, Massachusetts Institute of Technology (1998).
- [41] N. Wiener, The interpolation, extrapolation and smoothing of stationary time series, New York: Wiley, 1949.
- [42] W. H. Press, S. A. Teulosky, W. T. Vetterling, B. P. Flannery, *Numerical Recipes 3rd Edition*, Cambridge University Press, 2007.
- [43] C. A. Hagmann, A search for cosmic axions, Ph.D. Thesis, University of Florida (1990).